

Received July 19, 2019, accepted August 23, 2019, date of publication August 28, 2019, date of current version September 12, 2019.

Digital Object Identifier 10.1109/ACCESS.2019.2938041

# Concept for Continuously Tunable Output Filters for Digital Transmitter Architectures

CHRISTIAN SCHUSTER<sup>1</sup>, (Student Member, IEEE), LUKAS SCHYNOL<sup>1</sup>, ANDREAS WENTZEL<sup>2</sup>, (Member, IEEE), FLORIAN HÜHN<sup>2</sup>, ERSIN POLAT<sup>1</sup>, SÖNKE SCHMIDT<sup>1</sup>, (Student Member, IEEE), ROLF JAKOBY<sup>1</sup>, (Member, IEEE), WOLFGANG HEINRICH<sup>2</sup>, (Fellow, IEEE), AND HOLGER MAUNE<sup>1</sup>, (Senior Member, IEEE)

<sup>1</sup>Institute for Microwave Engineering and Photonics, Technische Universität Darmstadt, 64283 Darmstadt, Germany

<sup>2</sup>Ferdinand-Braun-Institut, Leibniz-Institut für Höchstfrequenztechnik, 12489 Berlin, Germany

Corresponding author: Christian Schuster (schuster@imp.tu-darmstadt.de)

This work was supported in part by the German Federal Ministry of Education and Research (BMBF) under Grant 16FMD02, and in part by the German Research Foundation and the Open Access Publishing Fund of Technische Universität Darmstadt.

**ABSTRACT** This paper presents a novel output filter approach for continuously frequency-tunable digital power amplifiers, suitable for future seamless and band-less applications in 5G, e.g. for cognitive radios (CR). The presented tunable output filter is based on a multi-bandstop lowpass response to regenerate the original microwave signal at the output of the digital amplifier stage by suppressing unwanted frequency components. Compared to conventional tunable bandpass solutions, it offers higher tunability, higher linearity, good power handling capability and moderate losses especially around the carrier frequency. A tunable power amplifier (PA) demonstrator consisting of a 4-stage digital GaN PA MMIC and the novel tunable filter, is designed and fabricated for a carrier frequency range from 1 GHz to 3 GHz. Tunability is achieved by using commercial barium strontium titanate (BST) varactors. Small signal measurements were performed to evaluate tunability and suppression capabilities of the novel filter structure, which reveal a frequency tunability of 67 % with a suppression level of at least 13 dB for the undesired frequency components. The proposed filter structure exhibits a linearity over the tuning range with an OIP3 between 66 dBm to 70 dBm and high power handling capability. Finally, the performance analysis of the tunable PA demonstrator shows a peak efficiency of 70 %. Due to frequency limitations of the used PA stage, the efficiency slowly degrades to 20 % at the upper frequency band edge. Simultaneously, the output power varies between 27 dBm to 31 dBm.

**INDEX TERMS** Tunable circuits and devices, microwave power amplifiers, digital amplifiers, GaN, tunable filters, BST.

## I. INTRODUCTION

Upcoming 5G networks [1], [2], Internet-of-Things devices [3] and autonomous traffic [4] already create a steady growth of network nodes as well as an increased need for bandwidth in the wireless network and will continue to do so in future. This causes the electromagnetic spectrum to be an expensive resource which must be used as efficiently as possible [5]. Today's spectrum usability is limited by the traditional fixed spectrum assignment policy that allocates a large part to licensed users, leaving only the industrial, scientific and medical (ISM) radio bands for unlicensed use.

The associate editor coordinating the review of this article and approving it for publication was Yongle Wu.

The utilization of the licensed channels varies between unused but reserved frequency bands up to heavily used frequency channels e.g. digital video broadcasting (DVB), mobile communication services such as for long-term evolution (LTE) or the global system for mobile communication (GSM) [6]. The ISM bands around 2.4 GHz and 5 GHz are highly utilized by a huge number of services e.g. Bluetooth, W-LAN, HIPERLAN and ZigBee but offer only a rather limited bandwidth. To increase the spectrum efficiency, unused spectrum has to be released to services which are highly used. Therefore, autonomous capabilities for self-configuration and self-resilience has to be implemented in future networks. Dynamic spectrum management and seamless or band-less applications such as cognitive radio (CR)

systems and software-defined radios (SDRs) have been proposed to use underutilized licensed spectrum (whitespace). Such systems require a continuously reconfigurable analog RF front end, which is not bounded by predefined services and frequency channels [7]–[9].

Particular attention must be paid to the power amplifier (PA) in the RF front-end, as it mainly influences the overall efficiency with a total power consumption of approximately 43 % for a micro base transceiver station ( $\mu$ BTS) [10]. Moreover, the increasing number of base transceiver stations and multi-user multiple-input and multiple-output (MIMO) systems will relax the required PA output power but tightens the requirements regarding efficiency, cost and compactness. Today's solutions to overcome these challenges are load modulation e.g. Doherty [11], or supply modulation concepts, such as envelope tracking [12]. A major disadvantage of such concepts, particularly in CR and SDR based systems, are bandwidth limitations [11] and form factor [12]. The most revolutionary concept in terms of efficiency and operating bandwidth is the digital microwave power amplifier [13], [14].

In Figure 1, the basic block diagram of a digital transmitter chain is presented. It includes a digital modulator, a digital PA stage and an output filter stage. The modulator generates the digital input stream for the PA, whereby, also power peaks at harmonic frequencies and quantization-noise are generated. The digital signal is amplified in the downstream PA stage and an in-series connected output filter restores the amplified signal. This is done by filtering the unwanted spectral components and the quantization-noise. As the digital PA approach is inherently broadband, the output reconstruction filter is the bottleneck of multiband and/or reconfigurable amplifier concepts. The representative reconstruction filters in state-of-the-art digital amplifiers are commonly non-tunable bandpass filters [15]–[20]. Initially the single-band digital PA was improved to a multi-band system by Wentzel et al. by implementing a dual-band [21] and later a tri-band [22] reconstruction filter. Thereby, the operating range is extended, however, care must be taken with the placement of the bands, as passbands can not be placed at the harmonics of the other bands. This limits the number and frequency configurations of the multi-band approach. All published digital PA realizations in the microwave domain did not apply any tunable filter concepts to make the amplifier reconfigurable for future CR and SDR applications. Recently, in [23] we presented the first continuously tunable digital power amplifier using a 1<sup>st</sup>-order bandpass (BP) filter as output stage, whereby the inherent advantages of the digital

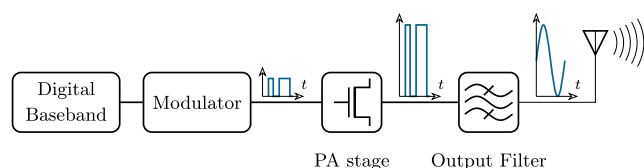


FIGURE 1. Block diagram of a digital transmitter chain.

PA approach concept could be preserved. That work reveals a tunable operating frequency between 1.1 GHz to 1.8 GHz, but shows low suppression of the harmonic power peaks, which reduces the signal quality. This could be improved by increasing the filter order which will consequently increase the losses in the passband, resulting in a decreased PA efficiency. Furthermore, the presented tunable PA shows only a tunability of 39 %, which is insufficient i.e. to cover a majority of the communication bands in the UHF band.

In this work, a novel filter approach with significantly improved tunability and moderate losses for a tunable digital transmitter branch is proposed to overcome these limitations. The targeted filter concept is based on the combination of a multi-bandstop and a lowpass filter for the suppression of harmonic power peaks. By using a suitable modulation technique with high signal-to-quantization-noise ratio (SQNR) [24], suppression of the quantization-noise becomes obsolete.

For the implementation of reconfigurability, different technologies can be used, such as micro electro mechanical systems (MEMS), microwave liquid crystal (LC) mixtures, semiconductors or ferroelectric materials. MEMS offer high linearity, power handling capability and low losses but suffer from comparatively lower tuning speed, tunability [25] and mechanical fatigue [26]. The microwave LC technology offers very high linearity, high power handling capability and low losses above 10 GHz [27]. Semiconductor devices offer high tunability and tuning speed, but suffer from low power handling capability and intrinsic low linearity [28], [29]. Ferroelectric materials such as barium strontium titanate (BST) have an E-field dependent permittivity and can be used for tunable microwave components. BST offers high linearity and power handling capability [30], [31] and is therefore a prime candidate for high-power applications such as RF power amplifiers. Furthermore, the continuous tuning [32] and low response time in the millisecond domain enables fast tuning of the PA stage which is necessary for frequency hopping. Therefore, commercial BST thin film varactors from STMicroelectronics are used as tunable elements in this work.

The paper is organized as follows. Section II introduces the digital power amplifier stage used in this work. Section III presents the novel output filter concept and its key parameters. The design of the tunable multi-bandstop lowpass filter is presented in Section IV, subdivided in lowpass and multi-bandstop theory, spurious passband suppression and final filter design. Section V covers the assembly of the tunable power amplifier demonstrator and, especially, of the tunable filter structure. Small and large signal analysis are performed in Section VI with regard to tunability, filter response behavior, nonlinearities, power handling capability, spectral behavior, output power, and efficiency. Section VII summarizes the findings of this paper and gives an outlook.

## II. DIGITAL GAN POWER AMPLIFIER STAGE

Figure 2 shows the schematic of the GaN-based digital voltage-mode power amplifier chip. The monolithic microwave integrated circuit (MMIC) is fabricated using

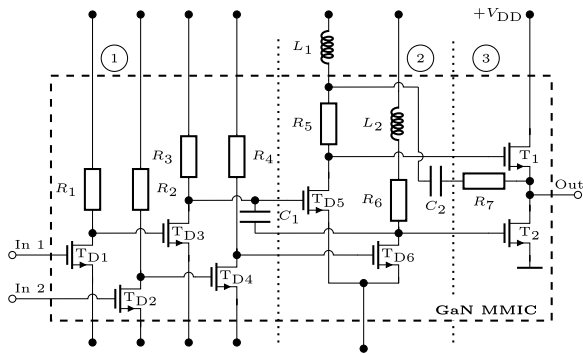


**FIGURE 2. Schematic of the digital GaN voltage-mode PA MMIC. It consists of a AB-class input stage (1) followed by the differential PA stage (2) and the push-pull final stage (3).**

the 0.25  $\mu\text{m}$  GaN-HEMT process line of the Ferdinand-Braun-Institut (FBH), Berlin, Germany. It is a 4-stage design including 8 GaN-HEMTs which achieves a voltage-gain of up to 40 dB and exhibits an area of 2.6 mm  $\times$  2.4 mm. The first stage (1) with  $T_{D1}$  and  $T_{D2}$  is operating in class-AB like mode amplifying the voltage swing  $V_{pp}$  of 0.75 V from the modulator output to a voltage swing of 5 V for the first digital stage ( $T_{D3}$ ,  $T_{D4}$ ). With this swing the transistors can be fully switched on by  $V_{gs} = 1\text{ V}$  or off by  $V_{gs} = -4\text{ V}$ . The differential PA in the next stage (2) generates the different input voltage swings required for the push-pull final stage (3) with  $T_1$  and  $T_2$ . The two final-stage transistors are 4  $\mu\text{m} \times 250\ \mu\text{m}$  in size and switch the output voltage on and off between  $V_{DD}$  and ideally 0 V according to the input signal. As a voltage is switched this type of digital circuit is denoted as voltage-mode configuration. Because no complementary GaN-HEMTs are available, the upper final-stage transistor  $T_1$  needs a very high voltage swing between  $-5\text{ V}$  to  $V_{DD}$  at the input while the lower one,  $T_2$ , requires a comparatively small voltage swing at the gate of only  $-5\text{ V}$  to 1 V. Thus, the efficient driving of the final-stage is very critical. The overall power-added efficiency (PAE) reaches around 50 % for a full-scale input PWM signal. This has been achieved by thorough optimization, such as using differential input signals for better switching, a feedback network formed by  $R_7$  and  $C_2$  and the external inductor  $L_1$ , which significantly reduces the applied voltage. Further work on improving overall efficiency of the digital PA stages has been published in [13], [33]. For the work presented here, only the final-stage drain efficiency  $\eta_{\text{drain}}$  is considered as an appropriate figure of merit for the potential of the proposed setup. The amplifier output impedance  $Z_{PA}$  at the carrier frequency depends on the utilized modulation technique as well as on maximum final-stage supply voltage  $V_{DD}$  and current  $I_D$  through  $T_1$  and  $T_2$ . Aiming for power levels in the range of 31 dBm and using a modulation scheme with maximum coding efficiency such as PWM leads to an optimum PA impedance of  $Z_{PA}(f_c) \approx 43\ \Omega$ .

### III. CONCEPT FOR TUNABLE OUTPUT FILTERS

The block diagram in Figure 1 shows the basic setup of a digital transmitter chain. The digital modulator is fed by a

multi-bit digital signal, which is defined by the carrier frequency  $f_c$  and its bandwidth  $B_c$ , that generates the one bit input stream for the PA stage. The in-series connected output stage restores the carrier signal by filtering the unwanted harmonic power peaks at  $nf_c$ ,  $n \in \mathbb{N}$ ,  $n \geq 2$  of the carrier frequency  $f_c$  and the quantization-noise. Ideally, all the power of the harmonics should be reflected back into the amplifier, as it can be recycled by the same and will increase the efficiency of the overall system. The output signal quality relates to the amplifier signal to noise ratio  $\text{SNR}_{\text{out}}$ , which defines the maximum output power level  $P_N$  of the unwanted frequency components, whereas the applied modulation technique defines the number and position of harmonics and the shape and level of the modulation-induced quantization-noise. Figure 3 presents the normalized power density spectrum of a state-of-the-art  $\Delta\Sigma$ -modulation scheme tailored to digital PA operation. The spectrum reveals harmonic power peaks at  $f_n = (2n - 1)f_c$  and a SQNR lower than 20 dB.

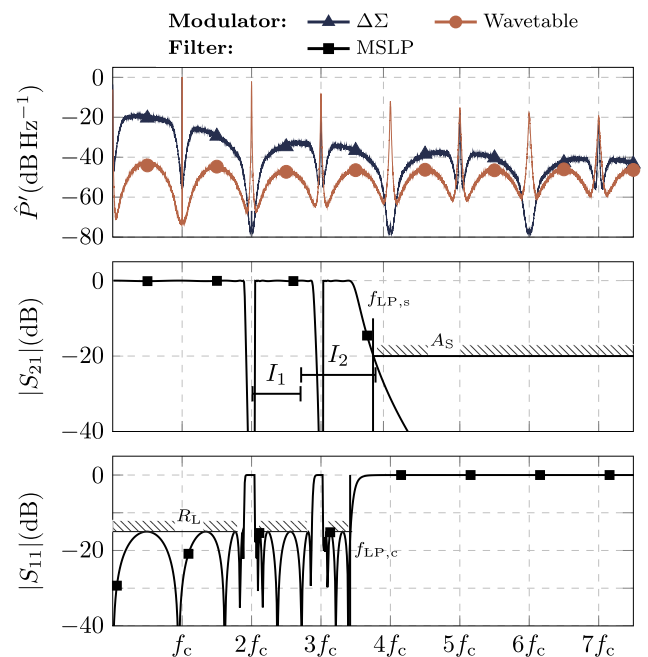


**FIGURE 3. The top graph presents the normalized power density spectrum  $\hat{P}'$  of a state-of-the-art  $\Delta\Sigma$ -modulator and of a wavetable based modulation technique presented by Hühn et al. in [24]. The lower graphs present the multi-bandstop lowpass filter response for a operating frequency range from 1 GHz to 3 GHz. The filter parameters are introduced in Section III.**

As mentioned non-tunable bandpass filters are commonly used as output stage for digital power amplifiers to filter out the wanted fundamental signal. Seamless tunability can be enabled, for example by continuously tunable bandpass filters. Cavity filter as in [34] exhibit losses below 1 dB and significant tuning capabilities. These are accomplished by changing the filter geometry, however, utilization of mechanical actuators limit their use in compact devices and are susceptible to mechanical failures. Planar filter implementations based on semiconductors, MEMS and ferroelectrics offer a

**TABLE 1.** Comparison of continuously tunable filters in the UHF band.

Diodes	$\Delta f$ [GHz]	$\tau_{f_0}$ [%]	IL [dB]
[39]	0.6 - 1.71	65	4.2 - 2.5
[40]	0.94 - 2.44	61	0.8 - 4.2
[41]	1.7 - 2.2	23	2.0 - 1.6
<b>MEMS</b>			
[42]	1.5 - 2.5	40	2.0-1.9
[45]	0.4 - 3.0	87	6.8-3.2
<b>BST</b>			
[46]	1.4 - 2.0	30	2.2 - 2.87
[40]	1.55 - 2.02	23	1.1 - 3.7
[23]	1.1 - 1.8	39	0.6 - 2.5

compact realization – a selection of those is given in Table 1. Bandpass filters based on varactor diodes [35]–[40] can reach tunabilities up to 65%. However, semiconductor based filters suffer from nonlinearities, which are an inherent characteristic of diodes. This can be improved by back-to-back configuration on the expense of filter tunability [41]. Reconfigurable MEMS filter in the UHF-band [42]–[44] reach insertion losses under 2 dB but possess limited tunability up to 40%. In [45], the frequency tunability is greatly increased to 87% by parallelizing continuously tunable filters at the cost of higher complexity, size and insertion loss. Filters based on BST varactors [23], [40], [46]–[50] achieve tunability up to 40%. Even the continuously tunable 1<sup>st</sup> order BST bandpass filter in [23] shows only a limited tunability of 39% with losses between 0.6 dB to 2.5 dB. The drawback of tunable bandpass filters is their strong dependence on the resonator tunability of the underlying tunable element, which can only be overcome by increasing complexity. This means, to reach a frequency tunability higher than the varactor’s tunability, a switched configuration between multiple tunable elements per resonator is required. Furthermore, important parameters as power-handling, losses and linearity are directly limited by the tunable elements at the resonators. Therefore, filters with tunable resonating elements at the operating frequency have to be avoided.

One prime candidate are multi-bandstop filters, which offer high suppression of the harmonic power peaks but no attenuation of the quantization-noise. By choosing a suitable modulation method with comparatively high SQNR, suppression of the quantization-noise is not absolutely mandatory. In the work by Hühn *et al.* [24], a new wavetable based modulation technique is presented. The overall SQNR is increased to approximately 40 dB at the expense of a higher number of harmonic power peaks at  $f_n = nf_c$ , see the normalized power density spectrum in Figure 3. Consequently the quantization-noise does not need to be suppressed by the output stage but in comparison to a  $\Delta\Sigma$ -modulation, double the number of harmonics have to be filtered out. With respect to the SNR<sub>out</sub> requirements, all harmonic power peaks above the maximum allowed power level  $P_N$  have to be suppressed by the multi-bandstop filter. In terms of a reconfigurable output stage,

the  $M_t$  stopbands at  $f_{t,k}$  of the filter have to be tunable. The operating range  $\Delta f_c$  of the reconfigurable PA system is given by

$$\Delta f_c = f_{c,\max} - f_{c,\min}, \quad (1)$$

and the resulting frequency tunability can be calculated to

$$\tau_{f_c} = \frac{f_{c,\max} - f_{c,\min}}{f_{c,\max}}, \quad (2)$$

where  $f_{c,\max}$  is the maximum and  $f_{c,\min}$  is the minimum operating frequency. Thus, the tuning range of the harmonic power peaks is increasing with the order  $n$  to

$$\Delta f_n = n\Delta f_c, \quad (3)$$

which also increases the tunability requirements for the multi-bandstop. To limit these requirements and the number of tunable stopbands, the bandwidth of the PA system is limited to the maximum operating frequency  $f_{c,\max}$ . Therefore, a lowpass (LP) filter is connected in series to suppress all harmonics above the stopband edge frequency  $f_{LP,s}$  with the minimum stopband attenuation level of  $A_s$ . The maximum number of harmonic power peaks within the operating range is given to

$$M_h = \left\lfloor \frac{f_{LP,s}}{f_{c,\min}} - 1 \right\rfloor, \quad (4)$$

at the minimum operating frequency. The required number  $M_t$  of tunable stopbands and their frequency interval  $I_k = [f_{t,\min,k}, f_{t,\max,k}]$  can be computed on the basis of the available stopband tunability

$$\tau_{f_t} = \frac{f_{\max} - f_{\min}}{f_{\max}}, \quad (5)$$

which depends on the used tuning technology and resonator design. In order to allow for continuously tunable  $f_c$ , the whole frequency range from the second harmonic  $2f_{c,\min}$  to  $f_{LP,s}$  must be covered by the tunable stopbands. If one assumes adjacent placement of the stopband intervals, which are numbered by the index  $k$  beginning from  $2f_{c,\min}$ , the stopband frequency range is

$$\Delta f_{t,k} = \frac{2f_{c,\min}\tau_{f_t}}{(1 - \tau_{f_t})^k}, \quad (6)$$

which increases with  $k$ . However, suppression of all harmonic power peaks is not guaranteed if more than one harmonic lies within a single stopband tuning range. Adjacent placing is, therefore, only possible as long as  $f_{c,\min} \geq \Delta f_{t,k}$  holds. The index  $a$  of the last stopband which fulfills the condition is

$$a = \left\lfloor \frac{\log(2\tau_{f_t})}{\log(1 - \tau_{f_t})} \right\rfloor. \quad (7)$$

The starting frequencies  $f_{t,\min,k}$  of the following stopbands  $k > a$  are spaced in a fixed distance of  $f_{c,\min}$ , which leads to an stopband range overlap to ensure suppression. As a result, the number of required stopbands is calculated to

$$M_t = \left\lceil a + \frac{f_{LP,s}}{f_{c,\min}} - \frac{2}{(1 - \tau)^a} \right\rceil \quad (8)$$

and the resulting stopband tuning intervals can be given to

$$I_k = \begin{cases} \left[ \frac{2f_{c,\min}}{\hat{\tau}^{k-1}}, \frac{2f_{c,\min}}{\hat{\tau}^k} \right], & 1 \leq k \leq a \\ \left[ f_{c,\min} \frac{2 + (k-a)\hat{\tau}^a}{\hat{\tau}^a}, f_{c,\min} \frac{2 + (k-a)\bar{\tau}^a}{\hat{\tau}^{a+1}} \right], & a < k \leq M_t \end{cases} \quad (9)$$

where  $\hat{\tau} = 1 - \tau_{fi}$ . In a special case, the last stopband can be omitted if the following conditions hold:

$$f_{t,\max,M_t-1} \geq f_{LP,s}, \quad (10)$$

$$f_{t,\max,M_t-2} \geq \frac{M_h}{M_h + 1} f_{LP,s}. \quad (11)$$

Then, the number of necessary stopbands reduces by one. The bandwidth  $B_n$  of the harmonic power peaks increases with their order  $n$  to  $B_n = nB_c$ . The bandwidth  $B_{t,k}$  of each stopband relates to the highest order harmonic within the stopband tuning interval  $I_k$ , and is given by

$$B_{t,k} = B_c \left[ \frac{f_{t,\max,k}}{f_{c,\min}} \right]. \quad (12)$$

The LP cutoff frequency  $f_{LP,c}$  is defined by the minimum reflection  $R_p$  in the passband and is set to the maximum operating frequency  $f_{c,\max}$ . Note that  $f_{LP,s}$  directly relates to  $f_{LP,c}$  via the filter order and type of the lowpass. For the realization the LP cutoff frequency is set to be slightly higher than the maximum operating frequency, in order to compensate simulation and manufacturing tolerances,

$$f_{c,\max} \leq f_{LP,c}. \quad (13)$$

By operating the power amplifier in the frequency range  $\Delta f_c$  two different operation modes occur. In the first tuning mode **A**, where

$$f_{c,\min} \leq f_c < \frac{f_{LP,s}}{2} \quad (14)$$

holds, harmonic power peaks are within the operating frequency range and have to be suppressed by the output filter stage. The second tuning mode **B**, where

$$\frac{f_{LP,s}}{2} < f_c \leq f_{c,\max} \quad (15)$$

holds for the carrier frequency, all harmonics are suppressed by the stopband region of the LP filter. In this operating mode, all stopbands must be tuned as far as possible from the carrier frequency in order to minimize their influence on it.

As presented in this section, the aimed operating frequency range  $\Delta f_c$  and available stopband tunability  $\tau_{fi}$  results in the required number of tunable stopbands  $M_t$  to cover the frequency span. In other words, the frequency tunability  $\tau_{fc}$  can be expanded by increasing the number of tunable stopbands with a single varactor at each resonator. In comparison to a tunable bandpass filter solution, the proposed filter concept avoids tunable resonators with resonance at the carrier frequency. By this, the influence of the variable elements used in the resonators on the power handling capability, linearity and filter losses are reduced.

#### IV. TUNABLE MULTI-BANDSTOP LOWPASS

The aimed filter response can be achieved by cascading a multi-bandstop and a lowpass filter, see Figure 4. As this two-stage design results in increased space consumption and losses an integrated filter structure with a multi-bandstop lowpass (MSLP) response is aimed for. To our best knowledge, there is only one tunable filter with a MSLP response presented in literature [51]. However, it is unsuitable as output filter as it features absorptive stopbands whereas reflective stopbands are required to recycle power and increase efficiency as mentioned in section III. Furthermore, the filter is implemented in lumped components with a passband below 800 MHz. Therefore, a novel design is pursued in this work. As the operating frequency of the carrier is between 1 GHz and 3 GHz in this work, the filter is implemented in planar microstrip technology which allows high design flexibility. The integration is achieved via modifying a standard L-C ladder-type lowpass filter by adding several tunable resonators, which builds on the non-resonating node concept [52], [53]. Firstly, the design procedure of the former is briefly explained and afterwards, the multi-bandstop realization is discussed. Subsequently, small improvements are added to the design.

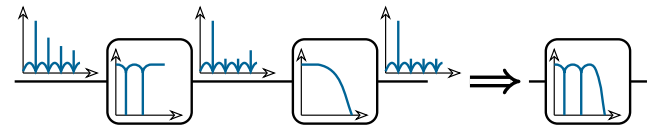


**FIGURE 4.** Filter concept for a multi-bandstop lowpass filter response, realized (left) by cascading a multi-bandstop and lowpass filter (right) by a single filter.

##### A. LOWPASS FILTER

As mentioned, basis for the LP is a  $N_{LP}$ -th order prototype L-C ladder, where  $N_{LP}$  is odd, with filter prototype element values  $g_i$  [54]. Here, odd-numbered  $g_i$  represent a lumped inductance, even-number  $g_i$  represent a lumped capacity. A Chebyshev prototype is suitable as it leads to a steep cut-off and symmetrical design. The series inductances with odd  $i$  are approximated by narrow transmission line segments as in the stepped-impedance filter approach [55]. Their length  $l_i$ , given a line impedance  $Z_1$  greater than the system impedance  $Z_0$ , can be calculated by

$$l_k = \frac{g_i Z_0}{\theta Z_1} \quad \text{with } \theta = \frac{2\pi f_{LP,c}}{v_{ph}}, \quad (16)$$

where  $f_{LP,c}$  is the design cut-off frequency of the lowpass,  $v_{ph}$  the phase velocity of the transmission line and the phase shift  $\theta$  at cut-off. Note that  $f_{LP,c}$  is chosen to be above the planned maximum carrier frequency  $f_{c,\max}$ , as required in (13), to account for the approximation error and ensure acceptable insertion loss in the whole carrier tuning range  $\Delta f_c$ . The parallel capacities  $C_i$  with even  $i$  are approximated by one-sided radial stubs connected at the line segment connections. For simplicity, their angle  $\alpha_{rad,i}$  and

input width  $w_{rad,i}$  is arbitrarily set and their length  $l_{rad,i}$  is such that the characteristic of a lumped capacity with

$$C_i = \frac{g_i}{2\pi f_{LP,c} Z_0} \quad (17)$$

is approximated in the frequency range below and near the lowpass cut-off. Utilization of radial stubs, in this case, allows for accurate control of the capacity for optimization purposes and avoids additional parasitic effects compared to the employment of lumped components. Another advantage is the realization of localized non-resonating, capacitive nodes with admittance  $Y_{node,i}$ , which can be easily modified in behavior. In Figure 5, the equivalent circuit is clarified. Furthermore, the ABCD-matrix can be obtained:

$$[A] = \begin{pmatrix} \cos(\beta l_1) & jZ_L \sin(\beta l_1) \\ j \sin(\beta l_1) / Z_L & \cos(\beta l_1) \end{pmatrix} \cdot \prod_{i=1}^{(N-1)/2} \left[ \begin{pmatrix} 1 & 0 \\ Y_{node,2i}(f) & 1 \end{pmatrix} \cdot \begin{pmatrix} \cos(\beta l_{2i+1}) & jZ_L \sin(\beta l_{2i+1}) \\ j \sin(\beta l_{2i+1}) / Z_L & \cos(\beta l_{2i+1}) \end{pmatrix} \right], \quad (18)$$

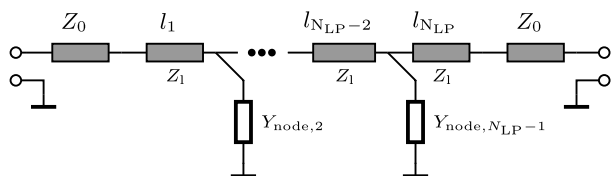


FIGURE 5. Equivalent circuit of the approximated L-C ladder with general nodes  $Y_{node,i}$  and transmission line segments with the length  $l_i$  and characteristic impedance  $Z_i$ .

where  $\beta$  is the phase constant on the line segments. Using conversion equations, the scattering parameters of the aimed filter structure can be computed. The stopband edge frequency  $f_{LP,s}$  can be acquired by simulations, which is required for the further filter design.

### B. TUNABLE MULTI-BANDSTOP

The stopband of the lowpass is primarily generated by the capacitive nodes, as  $\text{Im}\{Y_{node,i}(f)\}$  increases to infinity for rising frequency  $f$  for an ideal lumped capacitor. Consequently, the idea is that by placing admittance poles in  $Y_{node,i}$  at the harmonic frequencies  $f_n, n \leq 2$ , additional stopbands below the stopband edge frequency  $f_{LP,s}$  are created at those frequencies. The admittance of the radial stubs is close to zero in the same frequency region.

Admittance poles can be created by a basic capacitively loaded transmission line stub connected to a node. The stub line is characterized by a line impedance  $Z_t$  and length  $l_t$ . Tunability is achieved by employing a variable capacitor  $C_t$  with a minimum and maximum capacity  $C_{min}$  and  $C_{max}$ , respectively. The resonator design exhibits a low selectivity in its input impedance  $Z_{t,stub}(f)$  which would cause a large mismatch in the surrounding passband, decreasing the transmission of the carrier frequency. Hence, parametrization of

the resonator should maximize the selectivity. Numerically, one can show that when assuming a fixed  $Z_t$ , constant tunability  $\Delta C/C_{max}$  and fixed minimum resonance frequency by allowing  $l_t$  to change, the selectivity greatly increases for decreasing capacity values. Secondly, if the load capacitor is fixed instead of the line impedance, it can be derived that high  $Z_t$  enhance tunability of the resonance frequency and selectivity. Consequently, the line impedance is a trade-off between selectivity, tunability and bandwidth.

Selectivity of the impedance seen from the node can be further increased via decreasing the coupling strength by introducing a coupling capacitor in between. Here, the coupling capacities are implemented using interdigital capacitors (IDC) which individually connect each resonator stub to a node. A common approximation is a  $\pi$ -model with a transversal coupling capacitance  $C_c$  and two parasitic capacitances  $C_g$  to ground. A higher capacitance  $C_c$  leads to stronger coupling to the resonator increasing the bandwidth of the stopbands and signal suppression, however, passband mismatch also rises. Tunability decreases for decreasing coupling capacitance. Therefore, in this work, the minimum possible  $C_c$  which satisfies the required stopband suppression level is chosen. The stopband bandwidths  $B_{t,k}$  have to be set with respect to signal bandwidth  $B_c$  and its maximum resonance frequency  $f_{t,max}$ , see (12).

For the equivalent lossless circuit of a single coupled resonator, one can obtain the admittance

$$Y_{res}(f) = j2\pi f C_g + \left[ \frac{1}{j2\pi f C_c} + \frac{Z_{t,stub}(f)}{1 + j2\pi f C_g Z_{t,stub}(f)} \right]^{-1}. \quad (19)$$

Poles occur for frequencies  $f$  for which

$$0 = 1 + j2\pi f (C_g + C_c) Z_{t,stub}(f) \quad (20)$$

holds. The minimum and maximum resonance frequencies  $f_{t,min}$  and  $f_{t,max}$  are the solutions for  $C_t = C_{max}$  and  $C_t = C_{min}$  respectively, which must be numerically computed.

Multiple stopbands can be implemented by connecting multiple different stubs at a node in parallel. The admittance of the  $i$ -th LP node for  $M_t$  stopbands then becomes:

$$Y_{node,i}(f) = Y_{rad,i}(f) + \sum_{k=1}^{M_t} Y_{res,k}(f), \quad (21)$$

where  $Y_{rad,i}(f)$  is the admittance of the radial stub at the  $i$ -th node and  $Y_{res,k}(f)$  the admittance of the resonator creating the  $k$ -th stopband. The order of each tunable stopband is given by  $N_t = (N_{LP} - 1)/2$  if all filter nodes are used.

### C. STOPBAND IMPROVEMENT AND SPURIOUS PASSBAND SUPPRESSION

Due to the approximation utilizing distributed elements of the L-C ladder LP prototype, parasitic passbands are to be expected. Therefore, additional static admittance poles in the form of parallel  $\lambda/4$ -resonator stubs with line impedances  $Z_{s,i}$  and length  $l_{s,i}$  are added to the nodes, leading to further transmission poles which are used to suppress the parasitic

passbands. In particular, a resonator with resonance frequency closely above  $f_c$  improves the lowpass selectivity, especially if a variable stopband is tuned close to the cut-off frequency  $f_{LP,c}$ . The parameters of these additional stubs must be optimized using simulations.

Furthermore, the additional resonators at each node increase the effective node capacity, which decreases the lowpass cut-off frequency. As a result, the dimensions of the radial stubs must be corrected. Note that the self-resonance  $f_{rad,k}$  of the radial stubs also influences the upper-band behavior and can be utilized for parasitic passband suppression, thus, their parameters must be optimized in conjunction with the additional resonators.

**D. TUNABLE MULTI-BANDSTOP LOWPASS FILTER**

The specific filter of this work is designed for an operating range from  $f_{c,min} = 1$  GHz to  $f_{c,max} = 3$  GHz and its layout is presented in Figure 6.

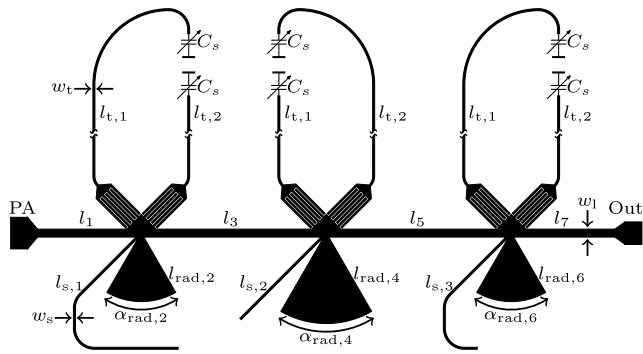


**FIGURE 6.** Layout of the multi-bandstop lowpass filter. The transmission line and radial stub dimensions can be found in Table 2. The dimensions of the tunable stubs are provided in Table 5, of the fixed-frequency stubs in Table 3 and the IDCs are described in Table 4.

A Chebyshev LP characteristic with 0.1 dB ripple level (return loss of 16.4 dB) of order  $N_{LP} = 7$  is used for the design process, the element values of the lowpass prototype are given in Table 2. In order to compensate the lumped-element approximation as well as tolerances and losses, the design cut-off frequency  $f_{LP,c}$  is chosen to be 3.5 GHz which is higher than  $f_{c,max}$ . The design system impedance  $Z_0$

**TABLE 2.** Chebyshev filter prototype values and dimensions of the lowpass filter.

Index	$i$	1, 7	2, 6	3, 5	4	Units
Element values	$g_i$	1.181	1.422	2.097	1.573	
<b>Inductor Segments</b>						
Line width	$w_1$	0.4	-	0.4	-	mm
Segment length	$l_i$	5.22	-	9.27	-	mm
<b>Radial Stubs</b>						
Angle	$\alpha_{rad,i}$	-	60	-	60	°
Input width	$w_{rad,i}$	-	0.25	-	0.25	mm
Length	$l_{rad,i}$	-	3.2	-	4.3	mm
Resonance freq.	$f_{rad,i}$	-	9.24	-	6.68	GHz

of the filter is set to the optimum amplifier impedance  $Z_{PA}$  of  $43 \Omega$ , see Section II. However, the output port of the filter is matched to  $50 \Omega$  by a tapered transmission line segment. The line impedance of the inductor segments  $Z_L$  of  $83 \Omega$  is a compromise between segment length and the accuracy of the inductor approximation. Longer segments increase node spacing, thus reducing the coupling between the shunt resonators. Using (16), the inductor segment lengths were obtained, and via (17) and simulations, the radial stub lengths  $l_{rad,k}$  were computed. Table 2 summarizes the optimized LP dimensions as well as the resonance frequency  $f_{rad,k}$  of the radial stubs.

The upper-band behavior was improved by adding one fixed resonator stub with length  $l_{s,i}$  and resonance  $f_{s,i}$  given in Table 3 next to the radial stubs to each of the nodes, which is in accordance to Section IV-C. Simulations then yield for a requirement  $A_s$  of 20 dB signal suppression a stopband edge frequency  $f_{LP,s}$  of approximately 3.8 GHz.

**TABLE 3.** Parameters of static resonator stubs.

Index	$i$	1	2	3	Units
Stub width	$w_{s,i}$	0.1	0.1	0.1	mm
Stub length	$l_{s,i}$	11.4	5.8	8.0	mm
Resonance frequency	$f_{s,i}$	4.2	8.4	6.1	GHz

A maximum of  $M_h = 2$  undesired harmonic power peaks can be expected within the LP-passband up to  $f_{LP,s}$ , thus, at least two tunable stopbands are necessary. The physical realization of these follows Section IV-B and aims for a high selectivity. Consequently, a characteristic impedance  $Z_t$  of  $134 \Omega$  is chosen for all tunable stubs. Fully electric tuning is achieved by implementing STMicroelectronic BST varactors *STPTIC15G2* as the capacitive load with tunable capacitance  $C_t$  in the range of about 0.3 pF to 1.9 pF. The interdigital coupling capacitors for each tunable resonator are designed to have a coupling capacitance  $C_c$  of 0.3 pF. This guarantees at least 20 dB suppression in the stopbands in simulation when a lossy model of varactor  $C_t$  is considered. The IDC dimensions are optimized in terms of required capacitance  $C_c$ , self resonance frequency and parasitic ground capacitance  $C_g$ . In Table 4, the IDC dimensions are listed which lead to a parasitic capacitance  $C_g$  of 0.17 pF.

**TABLE 4.** Dimensions of the interdigital capacities.

Parameters:	No. of fingers	Finger length	Finger width	Gap width
Units:		mm	$\mu\text{m}$	$\mu\text{m}$
Values:	7	1.98	80	80

The stub impedance, the varactor and the IDC considered above lead to a resonator tunability or stopband tunability  $\tau_{ft}$  of circa 29 % which is nearly independent of the resonator length  $l_{t,i}$ . Utilizing the procedure presented in Section III, one finds that the number of different necessary stopbands  $M_t$  is 2, which is sufficient to suppress all possible harmonics

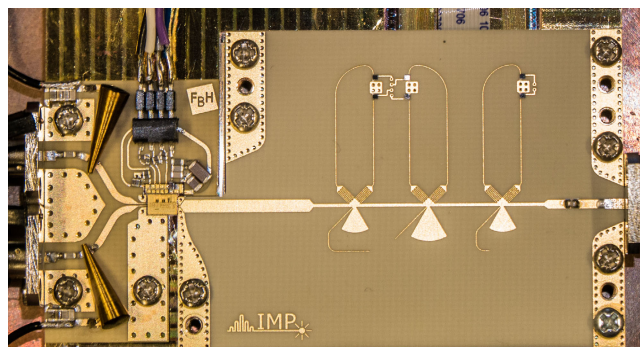
within the operating range. Thus two tunable stub resonators must be added to each node. Their frequency range intervals  $I_k$  have to be adjacent to each other with the interval of lower frequency starting at 2 GHz. By application of (20), the lengths  $l_{t,i}$  of the resonator stubs were designed, resulting in the dimensions and frequency ranges provided in Table 5.

**TABLE 5. Dimensions of the resonators and their calculated resonance frequency ranges for a given capacity range  $\Delta C_t$  of the tunable BST varactors.**

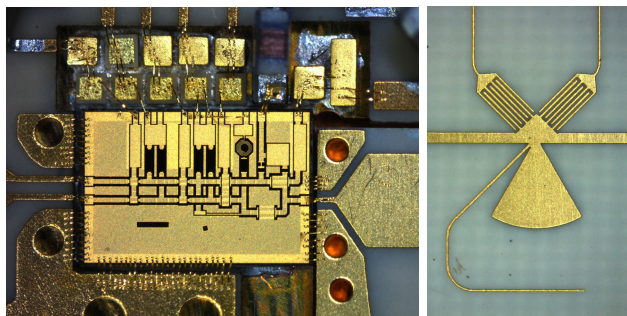
Index $k$	Parameters:	Width $w_t$ mm	Length $l_{t,k}$ mm	Calc. frequency range	
	Units:			$f_{t,min,k}$ GHz	$f_{t,max,k}$ GHz
1		0.1	19.4	1.94	2.72
2		0.1	11.1	2.71	3.83

## V. DIGITAL POWER AMPLIFIER DEMONSTRATOR

The digital power amplifier demonstrator is presented in Figure 7a and can be subdivided into three parts: 1) power amplifier input circuit and biasing network for the digital PA stage; 2) power amplifier stage built-up as a MMIC; and 3) output filter stage implemented as the tunable multi-bandstop lowpass filter structure. The components are connected using 25  $\mu\text{m}$  gold bond wires. The parasitic inductance is calculated to  $L_{\text{bond}} \approx 1 \text{ nH}$  [56], which is considered in the design of the microstrip to coplanar waveguide (CPW) transition, see Figure 7b right side. All components are mounted on a copper frame for cooling the PA stage and as solid



(a)



(b)

(c)

**FIGURE 7. (a) Complete fabricated digital PA System. (b) Power amplifier stage MMIC. (c) Close up of a filter node with connected IDCs, radial stub and resonators for spurious passband suppression.**

mechanical support. The overall PA demonstrator size is 70 mm  $\times$  40 mm  $\times$  10 mm.

The filter structure is fabricated on a three-layer circuit board with the cross section presented in Figure 8. The high frequency ceramic laminate Rogers RO4003C with a relative permittivity of  $\epsilon_r = 3.55$  and a layer thickness of 508  $\mu\text{m}$  is used as top substrate. The lower one is a standard FR4 substrate with a layer thickness of 200  $\mu\text{m}$ . A copper cladding of 17  $\mu\text{m}$  with a nickel palladium gold surface finish to enable wire bonding is used. The filter structure is processed on the top layer, which uses the middle layer as RF ground. The bottom layer is used for DC biasing the varactors on the top layer. For isolation, the bottom layer is covered by a standard solder mask. The manufactured filter structure is shown in Figure 7a and a close up of one filter node with connected IDCs is presented in Figure 7c. The BST thin-film varactor STPTIC-15G2 are used for the filter demonstrator. The RF ground and DC biasing are connected to the top layer by vias with a diameter of 200  $\mu\text{m}$  and 400  $\mu\text{m}$ , respectively. An overall filter structure area of 30 mm  $\times$  25 mm seems to be large compared to non-tunable surface acoustic wave (SAW) BP filter, but in contrast to static filters, a tunable filter concept enables the access to a large number of services within the tuning range  $\Delta f_c$ .

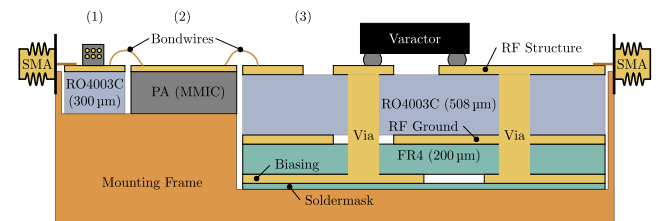


**FIGURE 8. Drawing of the cross section of the tunable digital power amplifier demonstrator. (1) PA input and biasing network, (2) power amplifier stage MMIC and (3) tunable multi-bandstop lowpass filter as output stage. (not to scale).**

## VI. MEASUREMENTS

The performance of the proposed tunable filter structure is evaluated under small signal and large signal conditions. The small signal analysis provides the filter's scattering parameters and tunability of the stopbands. Moreover, in the large-signal analysis the linearity and power handling capability of the filter structure have been checked. Furthermore, the output power  $P_{\text{out}}$  and final-stage drain efficiency  $\eta_{\text{drain}}$  of the tunable digital power amplifier system over the entire operating frequency range are presented. Additionally, the close-in and far-out spectral behavior of the PA system at different tuning states are shown. We have to emphasize that in this work only the final-stage drain efficiency of the tunable PA system is calculated and used as a figure of merit. As the PAE for the used PA is quite low (cp. Section II) and it is not optimized for modulated measurements, i.e., back-off operation, the  $\eta_{\text{drain}}$  characteristic is sufficient to check at least the feasibility of the targeted concept of a continuously tunable output filter with a digital PA stage.

**A. FILTER: SMALL SIGNAL ANALYSIS**

The small signal characteristics are evaluated in terms of tunability, insertion loss and return loss by measuring the scattering parameters. All S-parameter measurements were de-embedded at the input port and output port to the PA's optimum impedance of  $43\ \Omega$  and the load impedance of  $50\ \Omega$ , respectively. Thereby, hypothetical tuning scenarios are assumed with a carrier frequency  $f_c$  and harmonic power peaks at especially  $2f_c$  and  $3f_c$ . In a first step, measurements and simulations are compared and the filter stopband is evaluated up to 10 GHz.

The simulated and measured scattering parameters for a operating frequency  $f_c$  of 1 GHz are shown in Figure 9. Overall, the frequency response is of similar shape with a Chebyshev reflection ripple response near the design return loss of 16 dB, which is interrupted by the stopbands. The carrier is attenuated by 0.7 dB in measurements, 0.5 dB more than in simulation. Stopbands are positioned at the 2<sup>nd</sup> and 3<sup>rd</sup> harmonics with the first stopband measuring a suppression level of 13 dB and 23 dB for the second one. In simulation, over 20 dB attenuation is reached, however, the stopbands are wider in the measurements mainly due to a reduced resonator quality factor. The lowpass stopband edge frequency  $f_{LP,s}$  is measured to 3.9 GHz with a stopband attenuation  $A_s$  consistently above 20 dB up to 10 GHz.

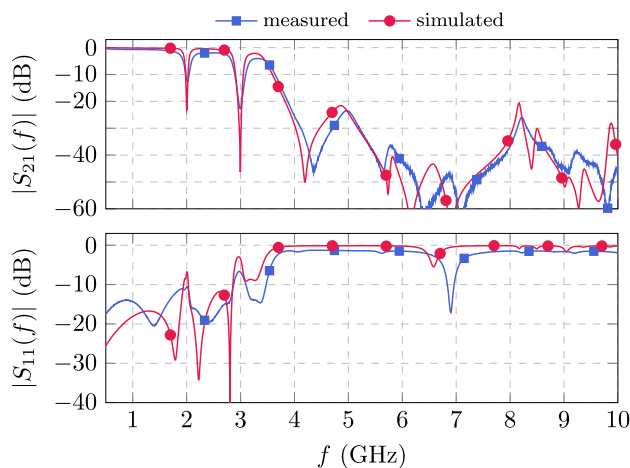


**FIGURE 9.** Simulated and measured scattering parameters of the minimum tuning state for a carrier frequency  $f_c$  of 1 GHz. The lowpass stopband edge frequency  $f_{LP,s}$  is measured to 3.9 GHz.

The filter is tuned by changing the bias voltage for the BST thin film varactors between 0 V to 24 V. Utilizing the whole biasing voltage range, measurements exhibit a minimum and maximum center frequency  $f_{t,min,1}$  and  $f_{t,max,1}$  from 1.94 GHz to 2.64 GHz for the first stopband, which is close to the calculated boundaries. The second one is tunable from  $f_{t,min,2} = 2.60$  GHz to  $f_{t,max,2} = 3.51$  GHz. A deviation of  $f_{t,max,2}$  compared to the calculated tuning range is expected due to frequency limitations of the applied varactors. The tunability of the first stopband is 26.5 % and of the second one 25.9 %.

Various measured tuning states for both tuning modes **A** and **B** are presented in Figure 10. In the first case, for a carrier frequency  $f_c$  of 1 GHz to 1.2 GHz (see Figure 10 top), two harmonic power peaks  $f_2$  and  $f_3$  are inside the LP passband and the corresponding tuning states are given. Clearly, the first stopband follows  $f_2$  from 2 GHz to 2.4 GHz with an attenuation in the range of 13 dB to 15 dB. Within the tuning range of the second stopband, more than 20 dB attenuation of  $f_3$  is accomplished. However, due to the reduced upper tuning bound  $f_{t,max,2}$ , it can not track  $f_3$  up to 3.6 GHz. Nevertheless, the LP itself suppresses  $f_3$  by 14 dB at this frequency. In the second case (see Figure 10 center), tuning states for  $f_c$  from 1.3 GHz to 1.8 GHz are demonstrated. Here, only the second harmonic  $f_2$  is below the cutoff  $f_{LP,s}$ . It is tracked by the second stopband up to  $f_{t,max,2}$  and, while tuning, is attenuated above 20 dB. Simultaneously, the first stopband is constantly tuned to its maximum resonance frequency  $f_{t,max,1}$ . For  $f_c = 1.3$  GHz, it is shown that both stopbands can be overlapped at 2.6 GHz, which increases the attenuation to 38 dB. In the last case (see Figure 10 bottom), no undesired harmonic is located inside the LP passband and exemplary tuning states for a carrier frequency of 2.0 GHz and 3.0 GHz are illustrated. The stopbands are tuned as far as possible from  $f_c$  to decrease mismatch at the signal frequency.

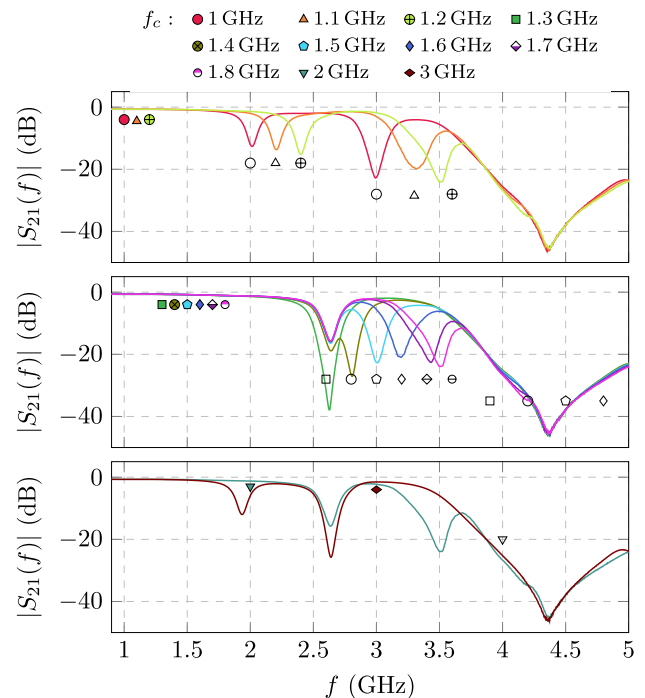


**FIGURE 10.** Measured tuning states for carrier frequencies from 1 GHz to 3.2 GHz. The upper two graphs correspond to the tuning mode **A** and the lower graph to mode **B**. The colored markers represent the carrier position at  $f_c$  and the unfilled markers the related position of the 2<sup>nd</sup> and 3<sup>rd</sup> harmonic.

Figure 11 summarizes the insertion loss at the carrier frequency  $f_c$ , upwards from 1.0 GHz in 100 MHz-steps, and the attenuation of the corresponding harmonics  $f_2$  and  $f_3$ . A low

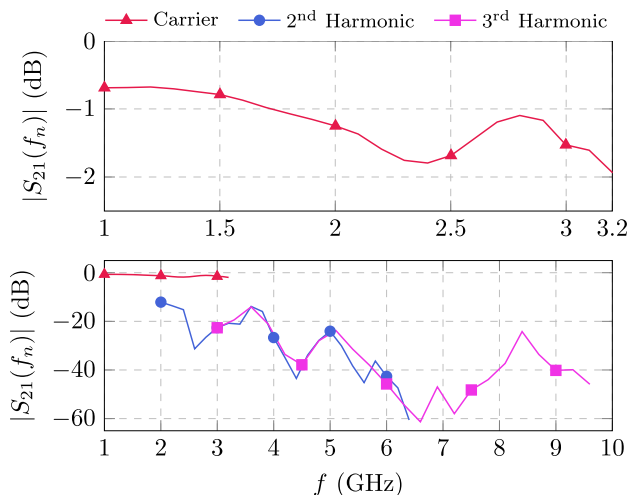


**FIGURE 11.** Measured transmission of the carrier and suppression of its 2<sup>nd</sup> and 3<sup>rd</sup> harmonic at  $f_2$  and  $f_3$ , respectively, for a carrier frequency  $f_c$  between 1 GHz to 3.2 GHz.

insertion loss, for tunable filters, between 0.7 dB to 2 dB at the carrier frequency is achieved up to  $f_c = 3.2$  GHz which leads to a slightly higher frequency range than designed. The main reason for the losses are the biasing dependent dielectric losses of the BST varactors and the quality factor of the interdigital capacitors. Attenuation of the harmonic power peaks does not always reach the targeted 20 dB, but is at least 13 dB for all measured tuning states. Overall, the measured carrier frequency tunability  $\tau_{fc}$  is, therefore, 68.7 %.

**B. FILTER: NONLINEARITIES**

Nonlinearity of a system is specified by the output OIP<sub>n</sub> or the input IIP<sub>n</sub> inter-modulation products. The measurements were performed by using a two tone test signal with a frequency spacing of 1 MHz. The measurement set-up consists of a signal source MXG N5182A, spectrum analyzer MXA N9020A from Keysight Technologies and a power amplifier BLMA 0818-20D from BONN Elektronik. To evaluate high linearity components the measurement set-up was linearized by the N7621B Signal Studio Software for Multitone Distortion from Keysight Technologies. A maximum linearization of the test equipment results in an upper limit of the measurement range of the OIP<sub>3</sub> of 75 dBm. The measured output OIP<sub>3</sub> of the multi-bandstop lowpass filter without the PA stage over the entire operating frequency tuning range is presented in Fig. 12. The observed varying OIP<sub>3</sub> level over the tuning range depends on the capacitance-voltage (C-V) relation of the tunable element [57], [58]. The filter structure shows an OIP<sub>3</sub> between 66.6 dBm to 70.4 dBm depending on the voltage configuration of the BST varactors and by this on the frequency tuning state. So, the filter is capable to handle the high output power levels of the amplifier.

For additional linearization, the input signal of the switching stage can be adapted as follows: The wavetable-based modulation presented in [24] generates inherent highly linear

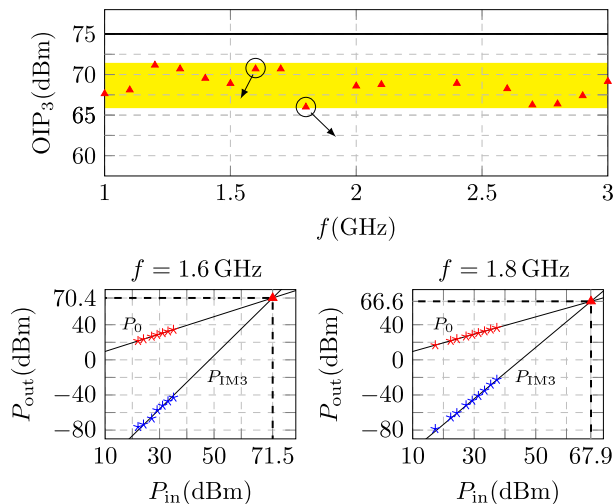


**FIGURE 12.** Measured OIP<sub>3</sub> of the filter over the center frequency tuning range. The lower two graphs present exemplary the output power of the fundamental  $P_0$  and the third order intermodulation product  $P_{IM3}$  over the input power  $P_{in}$  for the filter tuning states at 1.6 GHz and 1.8 GHz. The upper limit of the measurement range is a OIP<sub>3</sub> of 75 dBm.

input signals to the power amplifier. For example, for a 20 MHz WCDMA signal with a peak-to-average power ratio (PAPR) of 6.5 dB adjacent channel leakage ratios (ACLR) of more than 59 dB are easily reached at the input of the power amplifier. Moreover, the modulator also inherently provides the ability to correct for static non-idealities of the amplifier and the output filter. For this, the output after the filter is sampled and the actual amplitude and phase are compared to the ideal values. Initially, the amplitude values recorded in the wavetable for each waveform represent the ideal calculated system response of that specific waveform, which differ from the actual response. Thus, by replacing the amplitude values with the sampled ones the wavetable will provide a better representation of the actual behavior. Any deviations in phase can be added to the phase correction field. This is important for future work when modulated measurements will be conducted with a different optimized demonstrator which was not available up to now. In this work only single-tone measurements of the tunable PA system are performed to check the potential of such a set-up.

**C. FILTER: POWER HANDLING CAPABILITY**

The power handling capability of the tunable filter is investigated by large signal S-parameter measurements. The measured transmission coefficients  $|S_{21}|$  of the filter under power levels from 0 dBm to 40 dBm for the operating frequency state at 1 GHz are presented in Figure 13. As can be seen from the upper graph in Figure 13 the measured transmission coefficient reveals ripples, which are caused by the mismatch between the power amplifier and filter port impedance. The measurement system could only be response calibrated, due to the non-reciprocal nature of the measurement set-up. Besides the RF induced nonlinearity, increasing power levels

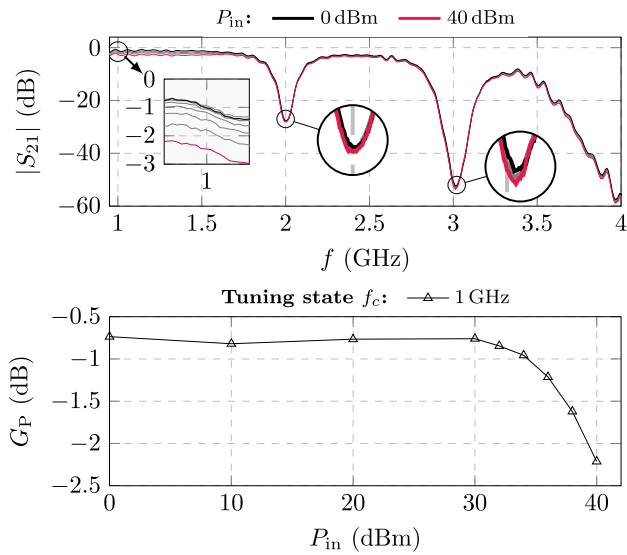


**FIGURE 13.** The upper graph shows the measured transmission coefficient  $|S_{21}|$  of the filter for power levels from 0 dBm up to 40 dBm of the filter for the tuning state at 1 GHz. The lower graph presents the operating power gain of the filter at 1 GHz.

can lead to self tuning, caused by heating of the tunable elements due to dielectric losses or by the RF E-field. The operation point can be held by compensating the self tuning by counter actively tuning the varactors, which will decrease the tuning range of the filter structure. The measured resonance positions of the two stopbands at 2 GHz and 3 GHz are only weakly affected by the applied RF power. Measurements over the entire tuning range reveals no self tuning at any power level up to 40 dBm. The operating power gain  $G_P$  of the filter, which is defined as the ratio between the output and input power of the filter, presented in Figure 13 stays constant up to input power levels of 30 dBm. For higher power levels the operating power gain gradually reduces. This effect can be attributed to thermal induced losses. The same behavior is reported for all tuning states. This proves the power handling potential of the filter prototype.

**D. TUNABLE PA SYSTEM: SPECTRAL BEHAVIOR**

In order to verify the performance of the reconstruction filter the input and output spectra of the tunable PA are analyzed at the tuning state at 1 GHz. For this reason the spectrum at the input of the PA is compared to the output spectra of the MSLP filter in an untuned and a tuned case. The untuned case represents the output spectrum only filtered by the fixed lowpass filter, since the tunable stopbands are tuned to frequencies other than the harmonics. For comparison, the output spectrum of the reconfigurable PA based on a tunable bandpass from [23] is presented. The spectra are shown in the upper graphs in Figure 14, the lower one presents a comparison of the presented spectra from the fundamental  $f_c$  up to the 6<sup>th</sup> order harmonics. The measurements of the MSLP in the untuned and tuned case reveal a static harmonic suppression of the 4<sup>th</sup> – 5<sup>th</sup> and the 6<sup>th</sup> – 9<sup>th</sup> harmonics above

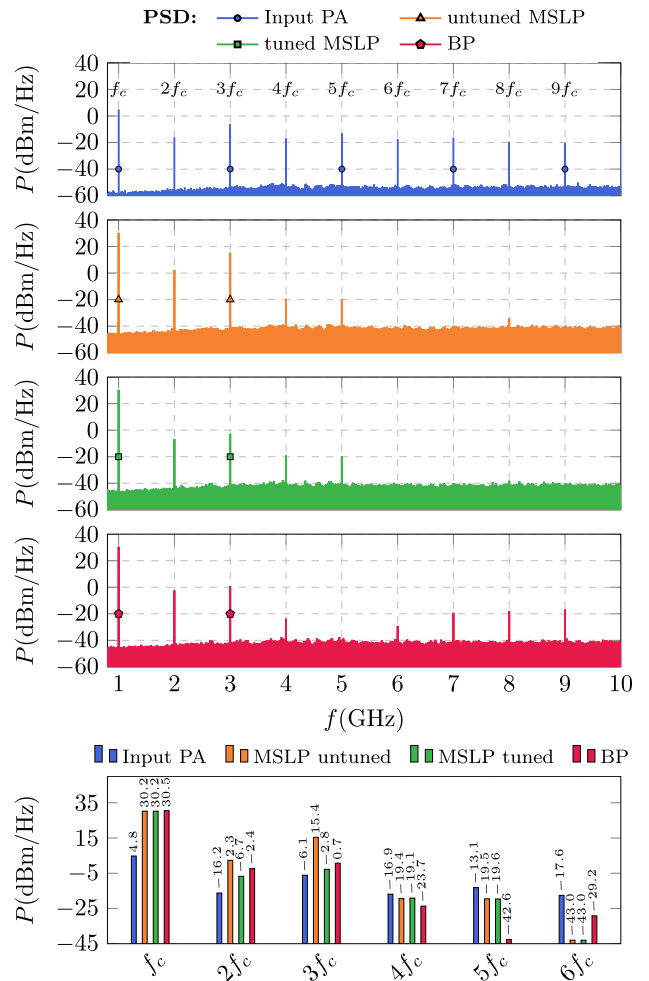


**FIGURE 14.** Measured far-out spectra at the input and output of the MSLP PA module in a tuned and untuned case and the output spectrum of the BP based PA module presented in [23]. The lower graph presents a comparison of the presented spectra from the fundamental  $f_c$  up to the 6<sup>th</sup> order harmonics. The measurements were performed with a resolution bandwidth RBW of 43 kHz and a video bandwidth VBW of 30 kHz.

50 dBc and 70 dBc, respectively, which are filtered out by the fixed lowpass filter. The tuned MSLP PA accomplishes a suppression of the 2<sup>th</sup> and 3<sup>rd</sup> harmonics above 36.9 dBc and 33 dBc, respectively. The suppression of the bandpass based PA in [23] shows a lower suppression of the 6<sup>th</sup> – 9<sup>th</sup> harmonics below 60 dBc, compared to the MSLP version. The 2<sup>nd</sup> and 3<sup>rd</sup> harmonic are suppressed by 32.9 dBc and 29.8 dBc, respectively. In comparison the MSLP based PA reveals at least 3 dB higher suppression of the 2<sup>nd</sup> and 3<sup>rd</sup> order harmonics compared to [23], which causes most of the distortions.

Figure 15 shows close-up views of the signal carriers at the output after the filter for 1 GHz, 2 GHz and 3 GHz input signal. The span around the carriers is 20 MHz each. One clearly recognizes the single-tone carriers and some small distortions arising around them, which are nearly 60 dBc below the peak. These occur due to signal distortions generated by the nonlinear behavior of the four PA stages.

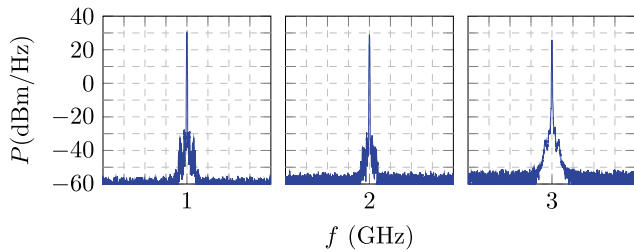


**FIGURE 15.** Close-up view of the measured spectra at the output of the realized demonstrator with a frequency span of 20 MHz at three frequency tuning states. The measurements were performed with a resolution bandwidth RBW of 51 kHz and a video bandwidth VBW of 430 Hz.

**E. TUNABLE PA SYSTEM: POWER MEASUREMENTS**

Large signal analysis has been carried out using a single-tone continuous wave (CW) signal at  $f_c$ . The digital input stream for the PA stage is modulated using the wavetable-based modulator approach from [24]. The signal is comparable to a pulse-width modulated signal with 50 % duty-cycle, which means a full-scale signal, i.e., the maximum input power at the signal frequency  $f_c$  is encoded. The input signal for the digital PA stage is generated by an arbitrary waveform generator (AWG) M8195A from Keysight Technologies which emulates the digital modulator, where the carrier frequency  $f_c$  is set by the used bit rate. The measurements were performed by varying the signal frequency between 1 GHz to 3 GHz and by applying a final-stage drain supply voltage  $V_{DD}$  of 20 V at the drain of the upper final-stage transistor  $T_1$  (cp. Figure 2). Figure 16 illustrates the measured output power and final-stage drain efficiency of the tunable digital PA demonstrator. At the filter output, the measured power  $P_{out}$  varies over the operating frequency range  $f_{c,min}$  to  $f_{c,max}$  between 27.0 dBm to 31.2 dBm. The final-stage drain efficiency  $\eta_{drain}$ , which is defined by

$$\eta_{drain} = \frac{P_{out}}{P_{DC,FS}}, \tag{22}$$

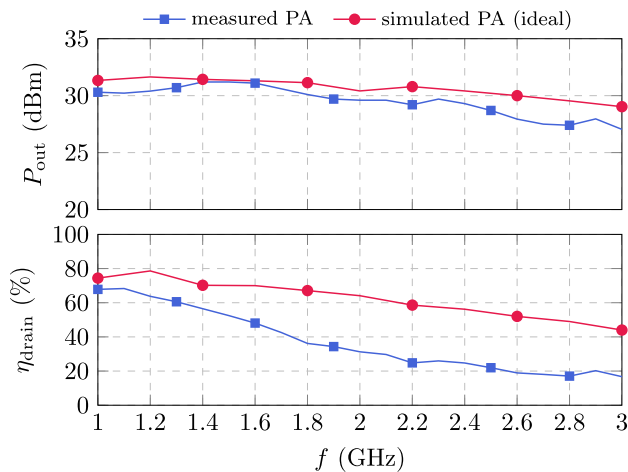


**FIGURE 16.** Measured output power  $P_{out}$  and drain efficiency  $\eta_{drain}$  of the tunable power amplifier. For comparison the simulation results of the used PA stage with an ideal bandpass output filter are presented.

where  $P_{DC,FS}$  is the final stage DC power, reduces from 70 % at  $f_{c,min}$  to 20 % at  $f_{c,max}$ . For comparison, simulations of the PA-stage with an ideal bandpass filter at  $f_c$  are presented. These reveal an output power in the range of 29 dBm to 31 dBm and an efficiency between 44 % and 77 %, respectively. One can clearly observe the same trend of decreasing output power and efficiency with increasing operating frequency as in the measurements. This is caused by the fact that decreasing pulse-width with increasing frequency leads to switching losses in the PA stages. The output capacitances of the transistors are charged and discharged in every switching event and additionally non-ideal switching transients gain importance [59]. Shorter pulses are more distorted in the four DC-coupled amplifier stages (cp. Figure 2) which may lead to a loss of single pulses. Moreover, the high sensitivity of the ten biasing points of the PA to small variations can cause distortions. Another reason for the performance degradation are trapping effects in the GaN transistors used. In digital operation the dynamic resistance  $R_{on}$  of the devices is much higher than usually when they have been driven with a pulse having a certain amplitude before. We have to state that, at the moment, this problem is not yet fully solved. Furthermore,  $P_{out}$  deviates between simulation and measurements at the upper operating frequency bound  $f_{c,max}$  by 2 dB which is caused by the filter losses.

**F. COMPARISON WITH OTHER WORKS**

The tunable MSLP PA approach is compared to fixed single-band, multi-band and a tunable PA module based on the same GaN PA MMIC from the FBH Berlin and to other single-band PA modules, see Table 6. Generally, the GaN MMIC based modules in [21]–[23], [60] reveal an output level in the range of 27 dBm to 38 dBm, while the CMOS based modules in [15], [17] offer power levels of approximately 20 dBm, which relates directly to the used technology. The single-band modules show drain efficiencies above 62 % where the module from [60] reports a maximum efficiency at 82 %. The multi-band concepts in [21], [22] increase the operating frequency range of the PA modules. However, the combination of possible frequency band combinations is limited, as passbands can not be placed at the harmonics of the other bands, e.g. 0.8 GHz and 1.8 GHz in [21]. This limits the number and frequency configurations of the multi-band approach. The recently published tunable PA in [23] covers a continu-

**TABLE 6.** Performance Comparison With Various PA Moduls.

	Type	$f_c$	$\eta_{drain}$	$P_{out}$
<b>This work</b>	continuous	1 – 3	70 – 20	30.3 – 27.7
[23]	continuous	1.1 – 1.8	73 – 44	30 – 29
[21]	dual-band	0.8, 1.8	75, 46	34.6, 33.8
[22]	tri-band	0.8, 1.6, 2.6	89, 56, 41	34, 31, 28
[60]	single-band	0.84	82	37.9
[17]	single-band	0.8	75	17
[15]	single-band	0.8	62	21

ous operating frequency range between 1.1 GHz to 1.8 GHz, which results in a tunability of 39%. In comparison this work accomplishes a operating frequency range between 1 GHz to 3 GHz – a tunability of 67%. Furthermore, the MSLP based PA reveals at least 3 dB higher suppression of the 2<sup>nd</sup> and 3<sup>rd</sup> order harmonics compared to the [23], which causes most of the distortions. In addition, the works [21]–[23], [60] reveal the same trend of decreasing drain efficiency at higher frequencies. As already mentioned this is due to the fact that higher switching frequencies and thus shorter pulses increase the losses due to frequency limits of the used technology (see previous section).

However, the first combination of a continuously tunable MSLP filter with a digital microwave power amplifier showing wide tuning range between 1 GHz to 3 GHz is of great importance as the very high potential of the setup has been proven. This makes the combination a true candidate for future 5G flexible networks.

## VII. CONCLUSION

A novel output filter concept for continuously tunable digital microwave power amplifiers has been presented for the first time. The tunable multi-bandstop lowpass filter approach allows very high frequency tunability of a digital PA. It can be easily extended by adding tunable stopbands, requiring only one tunable element per resonator. In contrast, the tunability of tunable bandpass filters can only be increased by complex switched configurations of multiple tunable elements at each resonator. Further, the presented filter concept avoids tunable resonators with resonance at the carrier frequency, which improves the power handling capability, linearity and filter losses. In order to validate the new concept, a reconfigurable PA module consisting of a digital GaN power amplifier and the aforementioned tunable output filter was fabricated. BST thin-film varactors from STMicroelectronics are used as tunable elements in the reconfigurable output stage. For the first time, a reconfigurable PA module has been realized which covers the frequency range from 1 GHz to 3 GHz. Measurements of the underlying multi-bandstop lowpass filter revealed an insertion loss at the carrier frequency between 0.7 dB to 2.0 dB over the entire operating range. Moreover, the tunable stopbands offer a suppression of the harmonic power peaks above 13 dB. The PA module full-scale output power ranges between 27 dBm and 31 dBm with a final-stage drain efficiency between 70% and 20%. In the frequency range below 1.5 GHz the efficiency stays above 50%. The frequency tunability of the digital PA of 67% documents the potential of the novel output filter stage approach. The continuous tunability enables access to all bands within the filter tuning range. Furthermore, the obtained reconfigurability, compactness and high efficiency of the digital power amplifier makes the approach an interesting candidate for future cognitive and software-defined radios. Future investigations will focus on modulated measurements of the tunable PA system by using a more robust and overall efficient PA stage.

## ACKNOWLEDGMENT

The authors would like to thank the Computer Simulation Technology AG for the provision of CST STUDIO SUITE®.

## REFERENCES

- [1] I. Selinis, K. Katsaros, M. Allayioti, S. Vahid, and R. Tafazolli, “The race to 5G era; LTE and Wi-Fi,” *IEEE Access*, vol. 6, pp. 56598–56636, 2018.
- [2] C. Campolo, A. Molinaro, A. Iera, and F. Menichella, “5G network slicing for vehicle-to-everything services,” *IEEE Wireless Commun.*, vol. 24, no. 6, pp. 38–45, Dec. 2017.
- [3] M. Wollschlaeger, T. Sauter, and J. Jasperneite, “The future of industrial communication: Automation networks in the era of the Internet of Things and industry 4.0,” *IEEE Ind. Electron. Mag.*, vol. 11, no. 1, pp. 17–27, Mar. 2017.
- [4] F. Qu, F.-Y. Wang, and L. Yang, “Intelligent transportation spaces: Vehicles, traffic, communications, and beyond,” *IEEE Commun. Mag.*, vol. 48, no. 11, pp. 136–142, Nov. 2010.
- [5] R. Gómez-García, J. P. Magalhães, J.-M. Muñoz-Ferreras, J. M. N. Vieira, N. B. Carvalho, and J. Pawlan, “Filling the spectral holes: Novel/future wireless communications and radar receiver architectures,” *IEEE Microw. Mag.*, vol. 15, no. 2, pp. 45–56, Mar./Apr. 2014.
- [6] T. Erpek, K. Steadman, and D. Jones, “Dublin ireland spectrum occupancy measurements collected on April 16-18, 2007,” Shared Spectr. Company, Vienna, VA, USA, Tech. Rep. 703-761-2818, Nov. 2007.
- [7] M. Helaoui, S. Boumaiza, and F. M. Ghannouchi, “Reconfigurable platform for software/hardware co-design of SDR base band pre-processing module,” in *Proc. Int. Symp. Antenna Technol. Appl. Electromagn. Can. Radio Sci. Conf.*, Jul. 2006, pp. 1–4.
- [8] R. Chen and H. Hashemi, “Reconfigurable SDR receiver with enhanced front-end frequency selectivity suitable for intra-band and inter-band carrier aggregation,” in *IEEE Int. Solid-State Circuits Conf. (ISSCC) Dig. Tech. Papers*, Feb. 2015, pp. 1–3.
- [9] J. H. Reed, J. T. Bernhard, and J.-M. Park, “Spectrum access technologies: The past, the present, and the future,” *Proc. IEEE*, vol. 100, pp. 1676–1684, May 2012. doi: 10.1109/JPROC.2012.2187140.
- [10] M. H. Alsharif, J. Kim, and J. H. Kim, “Green and sustainable cellular base stations: An overview and future research directions,” *Energies*, vol. 10, no. 5, p. 587, 2017.
- [11] S. Adhikari and K. Wu, “Developing one-dimensional electronically tunable microwave and millimeter-wave components and devices towards two-dimensional electromagnetically reconfigurable platform,” *Prog. Electromagn. Res.*, vol. 143, pp. 821–884, Jan. 2013.
- [12] C.-S. Yoo, Y. Liu, J. Fairbanks, P. Asbeck, P. Theilmann, and D. Kimball, “High efficiency multi-band envelope tracking power amplifier with tunable output frequency bands,” in *Proc. IEEE 16th Annu. Wireless Microw. Technol. Conf. (WAMICON)*, Apr. 2015, pp. 1–4.
- [13] F. Hühn, A. Wentzel, and W. Heinrich, “Highly compact GaN-based all-digital transmitter chain including SPDT switch for massive MIMO,” in *Proc. 48th Eur. Microw. Conf. (EuMC)*, Sep. 2018, pp. 918–921.
- [14] K. Motoi, A. Wentzel, M. Tani, S. Hori, M. Hayakawa, W. Heinrich, and K. Kunihiro, “Digital doherty transmitter with envelope  $\Delta\Sigma$  modulated class-D GaN power amplifier for 800 MHz band,” in *IEEE MTT-S Int. Microw. Symp. Dig.*, Jun. 2014, pp. 1–4.
- [15] T. P. Hung, J. Rode, L. E. Larson, and P. M. Asbeck, “Design of H-bridge class-D power amplifiers for digital pulse modulation transmitters,” *IEEE Trans. Microw. Theory Techn.*, vol. 55, no. 12, pp. 2845–2855, Dec. 2007.
- [16] T.-P. Hung, A. G. Metzger, P. J. Zampardi, M. Iwamoto, and P. M. Asbeck, “Design of high-efficiency current-mode class-D amplifiers for wireless handsets,” *IEEE Trans. Microw. Theory Techn.*, vol. 53, no. 1, pp. 144–151, Jan. 2005.
- [17] W.-Y. Kim, J. Rode, A. Scuderi, H.-S. Son, C. S. Park, and P. Asbeck, “An efficient voltage-mode class-D power amplifier for digital transmitters with delta-sigma modulation,” in *IEEE MTT-S Int. Microw. Symp. Dig.*, Jun. 2011, pp. 1–4.
- [18] A. Wentzel, C. Meliani, and W. Heinrich, “RF class-S power amplifiers: State-of-the-art results and potential,” in *IEEE MTT-S Int. Microw. Symp. Dig.*, May 2010, pp. 812–815.
- [19] R. Ma, “A review of recent development on digital transmitters with integrated GaN switch-mode amplifiers,” in *Proc. IEEE Int. Symp. Radio-Freq. Integr. Technol. (RFIT)*, Aug. 2015, pp. 73–75.

- [20] R. Hezar, L. Ding, J. Hur, and B. Haroun, "A 23 dBm fully digital transmitter using  $\Sigma\Delta$  and pulse-width modulation for LTE and WLAN applications in 45 nm CMOS," in *Proc. IEEE Radio Freq. Integr. Circuits Symp.*, Jun. 2014, pp. 217–220.
- [21] A. Wentzel, S. Chevtchenko, P. Kurpas, and W. Heinrich, "A dual-band voltage-mode class-D PA for 0.8/1.8 GHz applications," in *IEEE MTT-S Int. Microw. Symp. Dig.*, Jun. 2013, pp. 1–4.
- [22] A. Wentzel, M. Martinez-Mendoza, and W. Heinrich, "A compact tri-band GaN voltage-mode class-D/S PA for future 0.8/1.8/2.6 GHz LTE picocell applications," in *Proc. 10th Eur. Microw. Integr. Circuits Conf. (EuMIC)*, Sep. 2015, pp. 309–312.
- [23] A. Wentzel, C. Schuster, R. Jakoby, H. Maune, and W. Heinrich, "Reconfigurable GaN digital Tx applying BST bandpass filter," in *IEEE MTT-S Int. Microw. Symp. Dig.*, Jun. 2019, pp. 1484–1487.
- [24] F. Hühn, A. Wentzel, and W. Heinrich, "A new modulator for digital RF power amplifiers utilizing a wavetable approach," *Int. J. Microw. Wireless Technol.*, vol. 9, no. 6, pp. 1251–1260, Jul. 2017.
- [25] A. Abbaspour-Tamijani, L. Dusopt, and G. M. Rebeiz, "Miniature and tunable filters using MEMS capacitors," *IEEE Trans. Microw. Theory Techn.*, vol. 51, no. 7, pp. 1878–1885, Jul. 2003.
- [26] G. De Pasquale and A. Soma, "MEMS mechanical fatigue: Effect of mean stress on gold microbeams," *J. Microelectromech. Syst.*, vol. 20, no. 4, pp. 1054–1063, Aug. 2011.
- [27] H. Maune, M. Jost, R. Reese, E. Polat, M. Nickel, and R. Jakoby, "Microwave liquid crystal technology," *Crystals*, vol. 8, no. 9, p. 355, Sep. 2018.
- [28] X. Wang, P. Bao, T. J. Jackson, and M. J. Lancaster, "Tunable microwave filters based on discrete ferroelectric and semiconductor varactors," *IET Microw. Antennas Propag.*, vol. 5, no. 7, p. 776, 2011.
- [29] M. H. Norwood and E. Shatz, "Voltage variable capacitor tuning: A review," *Proc. IEEE*, vol. 56, no. 5, pp. 788–798, May 1968.
- [30] C. Schuster, A. Wiens, F. Schmidt, M. Nickel, M. Schüßler, R. Jakoby, and H. Maune, "Performance analysis of reconfigurable bandpass filters with continuously tunable center frequency and bandwidth," *IEEE Trans. Microw. Theory Techn.*, vol. 65, no. 11, pp. 4572–4583, Nov. 2017.
- [31] S. Preis, A. Wiens, N. Wolff, R. Jakoby, W. Heinrich, and O. Bengtsson, "Frequency-agile packaged GaN-HEMT using MIM thickfilm BST varactors," in *Proc. Eur. Microw. Integr. Circuits Conf. (EuMIC)*, Sep. 2015, pp. 440–443.
- [32] A. Kozyrev, A. Ivanov, V. Keis, M. Khazov, V. Osadchy, T. Samoilova, O. Soldatenkov, A. Pavlov, G. Koepf, C. Mueller, D. Galt, and T. Rivkin, "Ferroelectric films: Nonlinear properties and applications in microwave devices," in *IEEE MTT-S Int. Microw. Symp. Dig.*, vol. 2, Jun. 1998, pp. 985–988.
- [33] T. Hoffmann, A. Wentzel, F. Hühn, and W. Heinrich, "Novel digital microwave PA with more than 40% PAE over 10 dB power back-off range," in *IEEE MTT-S Int. Microw. Symp. Dig.*, Jun. 2017, pp. 2037–2040.
- [34] M. D. Sinanis, M. Abdelfattah, M. Cakmak, and D. Peroulis, "A 2.2–4.2 GHz low-loss tunable bandpass filter based on low cost manufacturing of ABS polymer," in *Proc. IEEE 19th Wireless Microw. Technol. Conf. (WAMICON)*, Apr. 2018, pp. 1–4.
- [35] Y.-C. Chiou and G. M. Rebeiz, "A tunable three-pole 1.5–2.2-GHz bandpass filter with bandwidth and transmission zero control," *IEEE Trans. Microw. Theory Techn.*, vol. 59, no. 11, pp. 2872–2878, Nov. 2011.
- [36] L. Gao and G. M. Rebeiz, "A 0.97–1.53-GHz tunable four-pole bandpass filter with four transmission zeroes," *IEEE Microw. Wireless Compon. Lett.*, vol. 29, no. 3, pp. 195–197, Mar. 2019.
- [37] Y. B. Zhang, F. L. Yu, and X. Y. Zhang, "Design of center frequency and bandwidth tunable bandpass filter," in *Proc. Int. Conf. Microw. Millim. Wave Technol. (ICMMT)*, vol. 5, May 2012, pp. 1–4.
- [38] C. Karpuz, G. B. F. Unuk, and P. Ö. Özdemir, "Design of dual-mode tunable filter surrounded by an electrical wall to obtain shielding effect," in *Proc. 47th Eur. Microw. Conf. (EuMC)*, Oct. 2017, pp. 25–28.
- [39] F. Lin and M. Rais-Zadeh, "A tunable 0.6 GHz–1.7 GHz bandpass filter with a constant bandwidth using switchable varactor-tuned resonators," in *IEEE MTT-S Int. Microw. Symp. Dig.*, May 2015, pp. 1–4.
- [40] X.-G. Wang, Y.-H. Cho, and S.-W. Yun, "A tunable combline bandpass filter loaded with series resonator," *IEEE Trans. Microw. Theory Techn.*, vol. 60, no. 6, pp. 1569–1576, Jun. 2012.
- [41] M. A. El-Tanani and G. M. Rebeiz, "A two-pole two-zero tunable filter with improved linearity," *IEEE Trans. Microw. Theory Techn.*, vol. 57, no. 4, pp. 830–839, Apr. 2009.
- [42] M. A. El-Tanani and G. M. Rebeiz, "High-performance 1.5–2.5-GHz RF-MEMS tunable filters for wireless applications," *IEEE Trans. Microw. Theory Techn.*, vol. 58, no. 6, pp. 1629–1637, Jun. 2010.
- [43] V. Sekar, M. Armendariz, and K. Entesari, "A 1.2–1.6-GHz substrate-integrated-waveguide RF MEMS tunable filter," *IEEE Trans. Microw. Theory Techn.*, vol. 59, no. 4, pp. 866–876, Apr. 2011.
- [44] A. J. Alazemi and G. M. Rebeiz, "A low-loss 1.4–2.1 GHz compact tunable three-pole filter with improved stopband rejection using RF-MEMS capacitors," in *IEEE MTT-S Int. Microw. Symp. Dig.*, May 2016, pp. 1–4.
- [45] K. Motoi, N. Oshima, M. Kitsunezuka, and K. Kunihiro, "A band-switchable and tunable nested bandpass filter with continuous 0.4–3 GHz coverage," in *Proc. 46th Eur. Microw. Conf. (EuMC)*, Oct. 2016, pp. 1421–1424.
- [46] M. K. Roy and J. Richter, "Tunable ferroelectric filters for software defined tactical radios," in *Proc. 15th IEEE Int. Symp. Appl. Ferroelectr.*, Jul./Aug. 2006, pp. 348–351.
- [47] C. Schuster, A. Wiens, M. Schüßler, C. Kohler, J. Binder, and R. Jakoby, "Hairpin bandpass filter with tunable center frequency and tunable bandwidth based on screen printed ferroelectric varactors," in *Proc. 46th Eur. Microw. Conf. (EuMC)*, Oct. 2016, pp. 1425–1428.
- [48] C. Schuster, P. Schumacher, M. Schüßler, A. Jiménez-Sáez, and R. Jakoby, "Passive chipless wireless pressure sensor based on dielectric resonators," in *Proc. IEEE SENSORS*, Oct./Nov. 2017, pp. 1–3.
- [49] Y. Zheng, M. Sazegar, H. Maune, X. Zhou, J. R. Binder, and R. Jakoby, "Compact substrate integrated waveguide tunable filter based on ferroelectric ceramics," *IEEE Microw. Wireless Compon. Lett.*, vol. 21, no. 9, pp. 477–479, Sep. 2011.
- [50] J. Nath, D. Ghosh, J. P. Maria, A. I. Kingon, W. Fathelbab, P. D. Franzon, and M. B. Steer, "An electronically tunable microstrip bandpass filter using thin-film barium-strontium-titanate (BST) varactors," *IEEE Trans. Microw. Theory Techn.*, vol. 53, no. 9, pp. 2707–2712, Sep. 2005.
- [51] D. Psychogiou, R. Gómez-García, and D. Peroulis, "Multi-functional low-pass filters with dynamically-controlled in-band rejection notches," in *IEEE MTT-S Int. Microw. Symp. Dig.*, May 2016, pp. 1–4.
- [52] A. Garcia-Lamperez and M. Salazar-Palma, "Single-band to multiband frequency transformation for multiband filters," *IEEE Trans. Microw. Theory Techn.*, vol. 59, no. 12, pp. 3048–3058, Dec. 2011.
- [53] D. Psychogiou, R. Gómez-García, and D. Peroulis, "Fully adaptive multiband bandstop filtering sections and their application to multifunctional components," *IEEE Trans. Microw. Theory Techn.*, vol. 64, no. 12, pp. 4405–4418, Dec. 2016.
- [54] G. Matthaei, E. M. T. Jones, and L. Young, *Microwave Filters, Impedance-Matching Networks, and Coupling Structures* (The Artech House Microwave Library). Dedham, MA, USA: Artech House, 1980.
- [55] D. M. Pozar, *Microwave Engineering*. Hoboken, NJ, USA: Wiley, 2012.
- [56] X. Qi, "High frequency characterization and modeling of on-chip interconnects and RF IC wire bonds," Ph.D. dissertation, Dept. Eng., Graduate Stud. Stanford Univ., Stanford, CA, USA Jun. 2001.
- [57] D. R. Chase, L.-Y. Chen, and R. A. York, "Modeling the capacitive nonlinearity in thin-film BST varactors," *IEEE Trans. Microw. Theory Techn.*, vol. 53, no. 10, pp. 3215–3220, Oct. 2005.
- [58] T. Sasaki and H. Hataoka, "Investigation of intermodulation in a tuning varactor," *IEEE Trans. Broadcast.*, vol. BC-29, no. 2, pp. 77–81, Jun. 1983.
- [59] F. H. Raab, P. Asbeck, S. Cripps, P. B. Kenington, Z. B. Popovich, N. Pothecary, J. F. Sevic, and N. O. Soka, "RF and microwave power amplifier and transmitter technologies—Part 2," in *Proc. High Freq. Electron. Copyright Summit Tech. Media*, Sep. 2003, pp. 1–9.
- [60] A. Wentzel, S. Chevtchenko, P. Kurpas, and W. Heinrich, "A flexible GaN MMIC enabling digital power amplifiers for the future wireless infrastructure," in *IEEE MTT-S Int. Microw. Symp. Dig.*, May 2015, pp. 1–4.



**CHRISTIAN SCHUSTER** (S'16) was born in Wiesbaden, Germany, in 1988. He received the B.Sc. and M.Sc. degrees from Technische Universität Darmstadt, Darmstadt, Germany, in 2012 and 2015, respectively, where he is currently pursuing the Ph.D. degree with the Microwave Engineering Group. His research interests include tunable microwave filters and reconfigurable RF transceiver systems.



**LUKAS SCHYNOL** received the B.Sc. degree in electrical engineering and information technology from Technische Universität Darmstadt, Germany, in 2019, where he is currently pursuing the M.Sc. degree in electrical engineering and information technology. His current research interest includes tunable planar microwave filters.



**ANDREAS WENTZEL** (M'16) received the Diploma and Ph.D. degrees in electrical engineering from the Technical University of Berlin, Germany, in 2006 and 2011, respectively. Since 2015, he has been the Head of the Digital PA Lab, III-V-Electronics Department, Ferdinand-Braun-Institut, Berlin, Germany. His research interests include design, realization and measurements of flexible digital Tx architectures, including advanced switch-mode power amplifier concepts realized on GaN and InP from GHz to sub-THz, as well as on optimized modulation schemes and filter structures suitable for this type of PAs. He is a member of MTT Society.



**FLORIAN HÜHN** received the Dipl.-Ing. degree in electrical engineering from the University of Bremen, in 2011. He is currently pursuing the Ph.D. degree with the Microwave Department, FBH. His research interests include modulators for highly efficient switch mode RF power amplifiers and digital microwave PA design.



**ERSIN POLAT** was born in Alzenau, Germany, in 1991. He received the B.Sc. and M.Sc. degrees from Technische Universität Darmstadt, Darmstadt, Germany, in 2014 and 2017, respectively, where he is currently pursuing the Ph.D. degree with the Microwave Engineering Group. His current research interests include tunable microwave filters and material characterization.



**SÖNKE SCHMIDT** (S'16) was born in Wiesbaden, Germany, in 1987. He received the M.Sc. degree in electrical engineering from Technische Universität Darmstadt, Germany, in 2015, where he is currently pursuing the Ph.D. degree with the Institute of Microwave Engineering and Photonics. His current research interests include microwave biosensors and dielectric spectroscopy.



**ROLF JAKOBY** (M'97) was born in Kinheim, Germany, in 1958. He received the Dipl.-Ing. and Dr.-Ing. degrees in electrical engineering from the University of Siegen, Germany, in 1985 and 1990, respectively. In January 1991, he joined the Research Center, Deutsche Telekom, Darmstadt, Germany. Since April 1997, he has been a Full Professorship with TU Darmstadt, Germany. He is currently a co-inventor of nine patents and participates on 11 awards in the last six years. His interdisciplinary research is focused on RFID, micro- and millimeter-wave detectors and sensors for various applications, and in particular on reconfigurable RF passive devices by using novel approaches with metamaterial structures, liquid crystal, and ferroelectric thick/thin film technologies. He is a member of the Society for Information Technology (ITG) of the VDE, the IEEE societies MTT, and AP. He is also an organizer of various workshops and a member of various TPCs. He has been the Chairman of the European Microwave Conference 2007 and the German Microwave Conference 2011. He is the Editor-in-Chief of FREQUENZ. In 1992, he was a recipient of the Award from the CCI Siegen, and in 1997, the ITG-Prize for an Excellent Publication in the IEEE TRANSACTIONS ON ANTENNAS AND PROPAGATION.



**WOLFGANG HEINRICH** received the Diploma, Ph.D., and Habilitation degrees from the Technical University of Darmstadt, Darmstadt, Germany. Since 1993, he has been with the Ferdinand-Braun-Institut (FBH), Berlin, Germany, where he is currently the Head of the Microwave Department and the Deputy Director of the institute. Since 2008, he has also been a Professor with the Technical University of Berlin. He was the President of the European Microwave Association (EuMA), from 2010 to 2018. He has authored or coauthored more than 350 publications and conference contributions. His current research interests include MMIC design with an emphasis on GaN power amplifiers, mm-wave integrated circuits, and electromagnetic simulation. He has been serving the microwave community in various functions.



**HOLGER MAUNE** (S'07–M'12) was born in Cologne, Germany, in 1981. He received the Dipl.-Ing. and Dr.-Ing. degrees in communications engineering from Technische Universität Darmstadt, Germany, in 2006 and 2011, respectively. His research interests include reconfigurable smart radio frequency (RF) systems based on electronically tunable microwave components, such as phase shifters, adaptive matching networks, tunable filters, duplexer, and multiband antennas. Their integration into system components, such as adaptively matched power amplifiers, reconfigurable RF front-ends, or fully integrated electronically beam-steering transceiver antenna arrays is in the focus of the work.

...